

# Design of a flexing organ-chip to model *in situ* loading of the intervertebral disc

Cite as: Biomicrofluidics 16, 054111 (2022); <https://doi.org/10.1063/5.0103141>

Submitted: 14 June 2022 • Accepted: 27 September 2022 • Published Online: 31 October 2022

 Jonathan P. McKinley,  Andre R. Montes,  Maple N. Wang, et al.



[View Online](#)



[Export Citation](#)



[CrossMark](#)

AIP Advances

Nanoscience Collection

READ NOW!

# Design of a flexing organ-chip to model *in situ* loading of the intervertebral disc

Cite as: Biomicrofluidics 16, 054111 (2022); doi: 10.1063/5.0103141

Submitted: 14 June 2022 · Accepted: 27 September 2022 ·

Published Online: 31 October 2022








View Online



Export Citation



CrossMark

Jonathan P. McKinley,<sup>1</sup>  Andre R. Montes,<sup>1</sup>  Maple N. Wang,<sup>2</sup>  Anuya R. Kamath,<sup>2</sup> Cissell Jimenez,<sup>1</sup> Jianhua Lim,<sup>2</sup> Siddharth A. Marathe,<sup>2</sup> Mohammad R. K. Mofrad,<sup>1</sup>  and Grace D. O'Connell<sup>1,a)</sup> 

## AFFILIATIONS

<sup>1</sup>Department of Mechanical Engineering, University of California Berkeley, Berkeley, California 94720, USA

<sup>2</sup>Department of Bioengineering, University of California Berkeley, Berkeley, California 94720, USA

<sup>a)</sup>Author to whom correspondence should be addressed: [g.oconnell@berkeley.edu](mailto:g.oconnell@berkeley.edu). URL: <https://oconnell.berkeley.edu>

## ABSTRACT

The leading cause of disability of all ages worldwide is severe lower back pain. To address this untreated epidemic, further investigation is needed into the leading cause of back pain, intervertebral disc degeneration. In particular, microphysiological systems modeling critical tissues in a degenerative disc, like the annulus fibrosus (AF), are needed to investigate the effects of complex multiaxial strains on AF cells. By replicating these mechanobiological effects unique to the AF that are not yet understood, we can advance therapies for early-stage degeneration at the cellular level. To this end, we designed, fabricated, and collected proof-of-concept data for a novel microphysiological device called the flexing annulus-on-a-chip (AoC). We used computational models and experimental measurements to characterize the device's ability to mimic complex physiologically relevant strains. As a result, these strains proved to be controllable, multi-directional, and uniformly distributed with magnitudes ranging from  $-10\%$  to  $12\%$  in the axial, radial, and circumferential directions, which differ greatly from applied strains possible in uniaxial devices. Furthermore, after withstanding accelerated life testing (66 K cycles of  $10\%$  strain) and maintaining 2000 bovine AF cells without loading for more than three weeks the AoC proved capable of long-term cell culture. Additionally, after strain ( $3.5\%$  strain for 75 cycles at  $0.5$  Hz) was applied to a monolayer of AF cells in the AoC, a population remained adhered to the channel with spread morphology. The AoC can also be tailored for other annular structures in the body such as cardiovascular vessels, lymphatic vessels, and the cervix.

Published under an exclusive license by AIP Publishing. <https://doi.org/10.1063/5.0103141>

## I. INTRODUCTION

Severe lower back pain is the leading cause of disability worldwide. In the United States, lower back pain affects  $70\%$ – $80\%$  of Americans<sup>1–3</sup> and costs  $\$100 \times 10^9$  annually;<sup>4</sup> yet, long-term treatment for lower back pain has been limited.<sup>5</sup> Of those patients with chronic lower back pain,  $40\%$  have internal disc disruption (IDD) or damage to the intervertebral disc as part of early disc degeneration.<sup>6</sup> Thus, to address the back pain epidemic, further investigation is needed into IDD and related intervertebral disc degeneration.

IDD is marked by radial fissures in the annulus fibrosus (AF), which is critical to spine health and function. The AF constrains the nucleus pulposus (NP), increasing intradiscal pressure, which allows the disc to withstand large compressive loads. Tears or fissures to the AF greatly increase internal strains. With additional loading, these tears are at risk of propagating further through the AF and triggering degenerative tissue remodeling.<sup>6–14</sup>

Moderate and severe degeneration has been noted with a decrease in disc height and water content and increased tissue fibrosis.<sup>15,16</sup> These changes lead to even greater AF strains and annular fissures, inducing the self-perpetuating degenerative cascade.<sup>12,17–23</sup>

The cause of IDD and the degenerative cascade is not well understood due to its multifactorial etiology stemming from both genetics and lifestyle. However, studies have recently pointed to cell-mediated, mechanobiological signaling as a potential initiator.<sup>24,25</sup> Therefore, cell-based experiments that model the complex strains specific to the disc are necessary to elucidate the role of disc mechanobiology in the degenerative cascade, thereby enabling drug development for lower back pain or tissue regeneration.

To this end, multiple 2D and 3D cell-straining studies have been conducted to characterize differences in cell signaling between normal and degenerated AF cells.<sup>24–26</sup> 2D studies impart uniaxial

tensile loads on monolayers of AF cells and monitor cellular structure, adhesion, and inflammatory response.<sup>21,27–29</sup> Efforts to investigate the effects of compressive loads in 3D microenvironments have focused on culturing AF cells in cell-laden gels, bioreactors, or hydrostatic pressure chambers before analyzing activity due to static or cyclic compression.<sup>26</sup> For each of these 2D and 3D studies, loading magnitude, type, and frequency are controlled, but only applied uniaxially either in compression or in tension. Microphysiological systems, or organ-chips, can model disease progression and repair. They can also apply more complex *in situ* loading modalities as demonstrated with the strain gradient generator for hydrogels created by Hsieh *et al.*<sup>30</sup> However, the miniaturization of AF complex strains in a microphysiological system has yet to be engineered academically or commercially, despite its relevance in disc degeneration.<sup>31–33</sup>

While conventional cell stretching studies offer the ability to isolate cell response from applied strain, the applied strains have limited physiological relevance given their over simplified configuration (e.g., uniaxial loading). Tissue-, or organ-culture models promise more physiologically relevant strains, but these approaches are complex and linking the multiaxial loading conditions to corresponding cell responses within a single tissue (e.g., AF within disc organ culture) is challenging. Understanding the link between disc mechanics and cell responses could allow for a more targeted strategy to address *in situ* disease initiation and propagation at the cellular level. Specifically, uncovering the distinctive cellular effects between uniaxial and multiaxial loading types is important because

it separates the unique contributions from both loading modalities to mechanobiological factors that potentially initiate the degenerative cascade. Therefore, there is a need for a more complete system that can isolate specific cell responses to loading conditions while maintaining physiological relevance.

Therefore, the objective for this study is to present a micro-physiological tool that can investigate the effects of physiologically relevant stretching of AF cells in 2D and 3D cultures. To achieve this goal, we designed, fabricated, and conducted initial testing of a flexing organ-chip that can apply either uniaxial or multiaxial stretching to AF cells secured within a single chamber [Figs. 1(a)–1(c)]. We developed our platform to mimic loading conditions applied to AF cells *in situ* by recapitulating proportional strains in the axial, radial, and circumferential directions [Fig. 1(d)]. In this proof-of-concept study, we provide preliminary experimental and computational data to demonstrate feasibility of our system, the flexing annulus-on-a-chip (AoC).

The novelty of the AoC lies in the highly physiologically relevant 3D strain made possible by bending an embedded chamber of cells, which better matches observed *in situ* strains in the AF.<sup>33</sup> This unique strain field integrated into a microfluidic platform satisfies an unmet need in intervertebral disc research,<sup>34</sup> which will enable new avenues for studying disease progression and regeneration. By combining the capabilities of a microphysiological system with the mechanical stimulus of an animal model, the AoC impacts intervertebral disc research by providing an improved research tool to study therapies for disc degeneration, which cannot

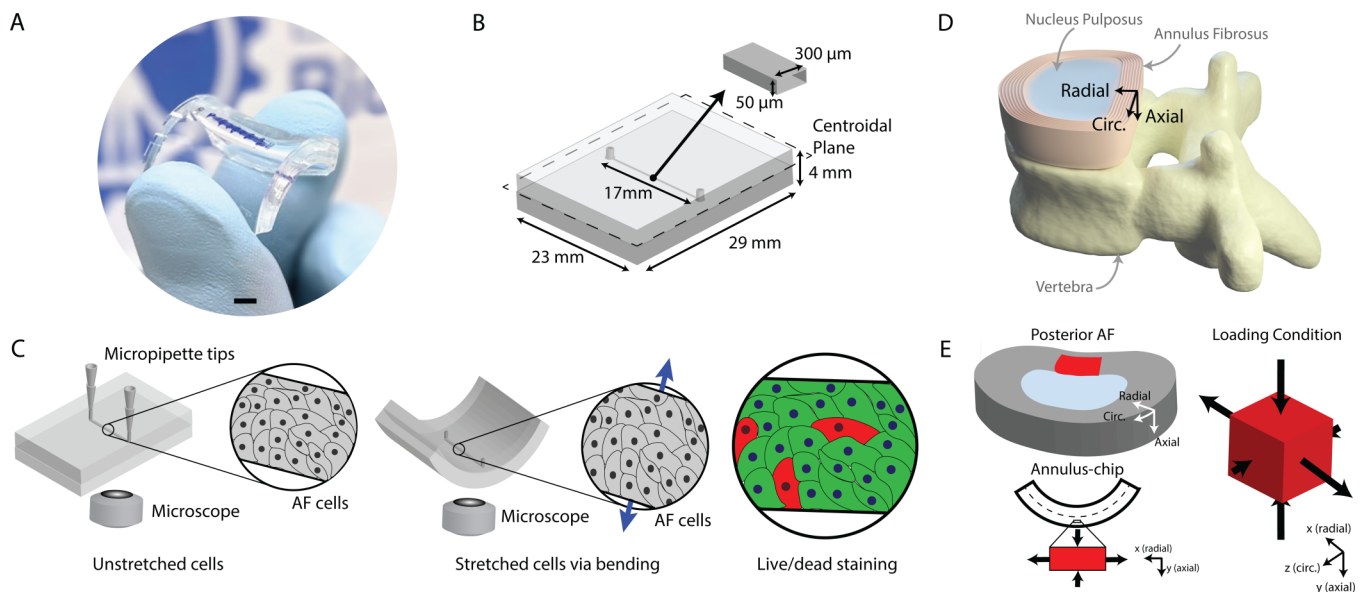


**FIG. 1.** (a) The AoC bent by hand to demonstrate the process of applying strain through device deformation. Blue markings in the channel are for reference only. Scale bar: 4 mm. (b) Schematic and dimensions of the AoC including the embedded channel. (c) Schematic showing the process of applying strain to cells in the channel by bending while the channel is imaged from below with an inverted microscope. (d) Schematic of vertebra and disc with positive axial, radial, and circumferential (or hoop) directions labeled. (e) When the posterior AF is under combined flexion, compression, and axial rotation, it assumes a state of strain where the axial and radial strains are inversely proportional and the circumferential strains are minimal and variable in comparison. This strain condition was replicated in the AoC channel when the device is flexed.

be studied to the same extent in conventional cell stretching devices. In this manuscript, we focus on highlighting the design work, the impactful intervertebral disc application, and the preliminary biological study behind the novel contribution of the device—complex loading that is physiologically relevant to the AF.

## II. RESULTS AND DISCUSSION

### A. AF physiological strain analysis to design the annulus-on-a-chip

Strains applied to the intervertebral disc are translated to the AF and NP.<sup>7</sup> Degeneration reduces internal pressure from the NP, increasing the magnitude of AF strains and the prevalence of tears.<sup>35,36</sup> When designing the AoC, we chose to replicate strains in a degenerated posterior AF<sup>12</sup> because of its susceptibility to tearing and initiating IDD.<sup>6</sup>

Much of the literature on AF mechanics has focused on uniaxial tissue stretching,<sup>35–37</sup> which applies large tensile strains in one direction and unconstrained contractile strains in the transverse directions due to the cell's Poisson's ratio. In contrast, *in situ* loading with additional boundary conditions results in more complex constraints that may increase the risk of AF tissue failure.<sup>38,39</sup> For example, under combined flexion, compression, and axial rotation, the posterior AF experiences inversely proportional tensile and contractile strains with low and variable circumferential strains.<sup>32,36,38</sup> By considering the strains on an “engineering element” within the posterior AF we can consider different strain ratios with respect to the orientation commonly used for the disc [e.g., axial:radial or circumferential:radial strain ratios; Fig. 1(e)]. These strain ratios make it possible to translate from whole disc loading of all types on one scale to strain on the smaller scale in the AF.

To create a target for strain orientation and proportionality for the AoC, we analyzed results from Amin *et al.*,<sup>32</sup> which evaluated axial, radial, and circumferential strains during the cyclic application of combined flexion, compression, and axial rotation on 12 degenerated discs (Pfirrmann grades II–III). We integrated the contributions from each strain direction by calculating strain ratios (axial:radial and circumferential:radial) across these discs at 20 000 cycles. The means and standard deviations were calculated from ratios of averaged strains to provide a physiological relevant strain window for the posterior AF. Circumferential:radial and axial:radial ratios were  $0.05 \pm 0.35$  and  $-0.95 \pm 1.17$ , respectively. The large standard deviations compared to the mean are due to the variation in circumferential strain directionality and not from variation in axial or radial strains. Ultimately, the AoC strain ratios were designed to fit within this physiologically relevant window by leveraging bending mechanics.

### B. Device design and development

Several microfluidic devices have been developed which apply complex strains to cells that are viewable under brightfield microscopes.<sup>34,40</sup> While these devices do not replicate the complex strains needed for the AF, their designs were referenced in the development of the AoC.

A device created by Hsieh *et al.* in 2014, for example, applies complex strains to annular hydrogel structures using unconfined

compression.<sup>30</sup> Concentric rings of hydrogel structures enable a gradient of complex strains. Compression is applied statically for simplicity. In 2019, Lee *et al.* also used unconfined compression on hydrogel structures but added dynamic loading to the device.<sup>41</sup> Arranged in an array, these hydrogel structures are cylindrical and can receive various magnitudes of compressive strains. The same year, another form of dynamic complex strain was developed on a cartilage-on-a-chip device by Occhetta *et al.*<sup>42</sup> This example uses rectangular posts along a  $300\ \mu\text{m}$  wide culture chamber to apply confined hyperphysiological compression. The culture chamber enables uniformity of applied strain by minimizing gradients as compared to the unconfined cylindrical structures.

Upon analysis of these existing microfluidic devices which apply complex strain, overarching design requirements for the AoC were established. The AoC needs a confined chamber like the cartilage-on-a-chip but one subject to bending to accomplish uniform physiological relevant strain. Like previous devices, the AoC also needs to be observable at all times during loading under a bright field microscope. Unlike previous devices, the AoC needs to be operational with or without a hydrogel to enable various types of modeling. Additionally, the AoC needs to be simple in both design and in operation to allow for the easy adoption of existing protocols performed on other microfluidic organ-chip platforms with small amounts of tissue, such as running polymerase chain reaction-enzyme-linked immunosorbent assays (PCR-ELISA), microscale Western blotting, or immunofluorescence imaging necessary for future biological work.

To satisfy these design requirements, the AoC became a deformable, optically clear, mechanically actuated organ-chip device that applies strains to cells through bending [Figs. 1(a)–1(c)]. The device was made of elastomeric polydimethylsiloxane (PDMS) with a  $300 \times 50\ \mu\text{m}^2$  channel created using standard soft lithography methods (further described in Sec. IV A).

The AF consists of alternating layers of fiber-reinforced tissue called lamellae. The  $300\ \mu\text{m}$  channel width was chosen to approximate the width of one lamellae (average lamellae thickness =  $420\ \mu\text{m} \pm 60\ \mu\text{m}$  in adults 53–76 years old).<sup>43</sup> The channel height ( $50\ \mu\text{m}$ ) was selected to be several times greater than the diameter of an AF cell ( $\sim 20\ \mu\text{m}$ ). As a result, cells have access to media and can be distributed along the channel length as they flow unobstructed. Meanwhile, the ratio of channel width to height was kept small (6:1) to limit the possibility of channel collapse during manufacturing and testing. FE simulations later showed a 6% decrease in mean channel height at the chip's maximum flexion state (Fig. S1A in the supplementary material), indicative of no channel collapse (Fig. S1B in the supplementary material).

Lastly, the channel length was chosen to be the longest possible to accommodate the greatest number of cells, minimize differences in strain along its length and fall within known lengths for nutrient diffusion in the AF. The AF relies on diffusion of nutrients and waste primarily through the disc's cartilaginous endplates given limited peripheral vasculature reaching only the outermost AF lamellae. Diffusion across the endplate alone results in a distance of at least 7–8 mm<sup>44</sup> with greater diffusion lengths by the time AF cells at the midheight of the AF are reached.<sup>15</sup> A half channel length of 8.5 mm, or 8.5 mm from the nearest port, falls within this physiological length for diffusion.

In total, the channel recapitulates a subunit of the AF at a much smaller scale than the whole disc. To account for this smaller scale, *in situ* whole disc loading, which includes a combination of axial and rotational loads, was converted to the multiaxial strains of different ratios (circumferential:radial and axial:radial) to be applied on the channel.

The device applied scalable and uniform strains on the channel when it was flexed over a rigid cylinder or barrel structure. The design of the cylinder and device thickness were made such that the axial, radial, and circumferential (or hoop) strains [Fig. 1(d)] were scaled to match physiological levels for the outer AF by repositioning the location of channel through the thickness of the PDMS device. In this design, radial and axial strains correspond to strains in the x- and y-directions, respectively [Fig. 1(e)]. For proof-of-concept testing, we kept the radius of curvature for the barrel constant and adjusted the location of the channel in the device to match strains observed in the posterior AF of degenerated discs. In the future, manufacturing could be simplified such that the channel location remains fixed while the extent of device bending dictates the applied strain.

Device flexing was achieved by powering servo motors that lifted the device’s edges while keeping the channel in the focal plane of the microscope [Figs. 2(a) and 2(b)]. During device development, the applied strain due to flexion was approximated using beam theory. Tensile radial strain ( $\epsilon_x$ ) was approximated using the device thickness ( $t$ ), barrel radius of curvature ( $r$ ), and the distance between the channel and the neutral axis ( $y_c$ ), which was assumed to be equivalent to the centroidal axis [Fig. 2(c)]. Thus, the applied radial strain increased linearly by moving the channel further from the neutral axis (along the negative y-direction) or by decreasing the radius of curvature,  $\rho$ ,

$$\epsilon_x = \frac{y_c}{\rho} = \frac{y_c}{r + \frac{t}{2}}$$

Lastly, long-term device durability against cyclic loading was assessed. We applied 10% strain at 0.5 Hz for 66 K cycles to represent a week-long cell based study. Cycle count was selected based

on daily activity. Rohlmann *et al.* measured a daily median of 4400 spine movements (most often in flexion) or  $\sim 30$  K movements each week.<sup>45</sup> To ensure that the AoC could withstand this week’s worth of loading cycles, an accelerated life test was performed for more than  $2\times$  the expected weekly loading cycles (66 K). Visual inspection of the AoC following accelerated life testing showed that the device was durable enough to withstand long-term cell-stretching studies and showed no signs of wear or fracture. The packing tape connecting the device to plastic cylinders connected to the servo motors exhibited subtle wear, but no signs of fracture. Servo motors and the apparatus to anchor each component remained intact.

### C. Comparing measured device strains to *in situ* physiological strains in the AF

To confirm that the AoC could recapitulate the complex strains within the posterior AF, we compared measured device strain ratios to those found in Amin *et al.*<sup>32</sup> To this end, two sets of five devices were fabricated using the first-order beam theory approximation (see Sec. IV C). While the device could be designed for higher peak strains (15%–20%) as seen in other cell studies,<sup>26–28,46</sup> initial device characterization and stretching process development was limited to 5%–10% strain based on the moderate to high physiological loading within the AF.<sup>26</sup> Measured applied strains in the x-direction were  $7.4 \pm 0.8\%$  and  $11.9 \pm 1.5\%$ , respectively. The relatively low standard deviation in the strains indicated that the device fabrication and loading was repeatable and robust.

As expected, measured strains were consistently higher than the first-order approximation. This suggested that a more comprehensive 3D computational model was needed to describe strain fields within the device. Additionally, this model could be used to determine axial and circumferential strains (see Sec. IV D), which are difficult to measure experimentally.

After modeling the 3D strain magnitude and orientation in the AoC, we calculated strain ratios within the channel to compare to the ratios in posterior AF tissue from degenerated human lumbar bone-disc-bone motion segments under flexion *in situ* (Table I). The standard deviations within the AoC’s ratios are due

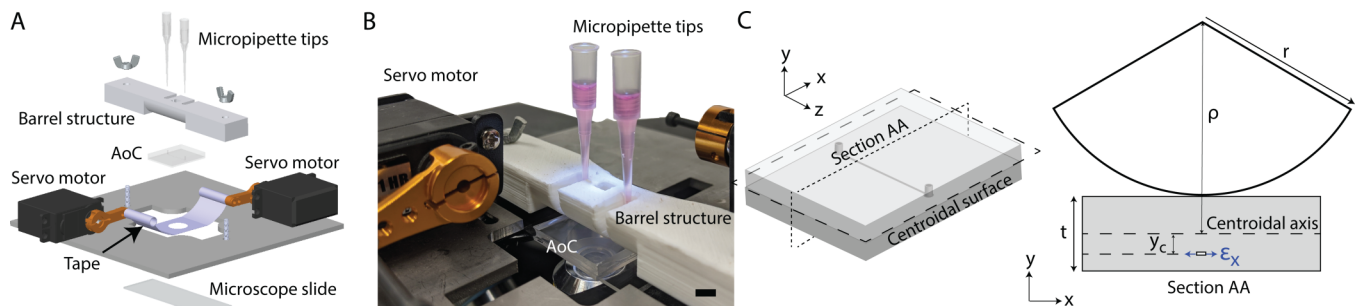


**FIG. 2.** (a) Exploded view of the experimental setup in SOLIDWORKS (overall dimensions:  $15 \times 15 \times 4.4$  cm<sup>3</sup>). (b) Representative image of the experimental setup. The AoC was held between a 3D printed barrel structure and a 1 mm thick glass slide placed on top of the microscope stage for imaging. Micropipette tips with equal volumes of cell culture media were plugged into ports at either end of the channel. A polypropylene “packing” tape was used to connect the device to servo motor horns and apply cyclic force on the device. As the servo horns rotated upward in tandem, the tape pulled tight, forcing the device to conform to the 3D printed barrel structure. Scale bar: 4 mm. (c) Cross section of the AoC with the relevant dimensions to compute the tensile strain,  $\epsilon_x$ , in the channel.

**TABLE I.** Comparison of strain ratios in the posterior AF within bone-disc-bone segments under flexion, the AoC, and commercial uniaxial cell stretchers.

	Circumferential:radial	Axial:radial
Posterior AF	$0.05 \pm 0.35^{32}$	$-0.95 \pm 1.17^{32}$
Annulus-on-a-chip	$-0.0025 \pm 0.07$	$-0.77 \pm 0.06$
Uniaxial cell stretcher <sup>a</sup>	n/a	$-0.55$ to $-0.4^{47}$

<sup>a</sup>STREX Cell (Strex Inc.).

to the variation along the length of the device channel. We considered the AoC as physiologically relevant since the circumferential:radial and the axial:radial ratios fit within the window of posterior AF ratios. Strain ratios for a conventional PDMS uniaxial cell stretcher were included to illustrate how physiological relevant loads cannot be achieved with a traditional cell stretching method that relies on the Poisson's effect of PDMS.

**D. Modeling device strains with finite element simulation**

While strains in the channel were measured optically in one direction (radial), a finite element (FE) analysis was used to verify

strain uniformity along the channel and assess strains in the other two directions. FE models were also used to assess strain heterogeneity, which can be used to alter the channel design for maximizing channel size and cell count. We developed models of three device configurations, with target strains of 0%, 5%, and 10% to validate our uniaxial strain measurements and establish the relationship between target strains throughout the bending cycle. We visualized the models' strain in the x-direction [Fig. 3(a)], which was considered to be the "radial strain" with respect to orientation in the AF [Fig. 1(e)]. Strains in the y- and z-directions correspond to axial and circumferential strains, respectively, and are labeled accordingly.

The FE results aligned well with our one-dimensional strain measurements taken under brightfield microscopy [Fig. 3(b)]. We then selected the "high strain" model (10% target) and varied the bending angle to achieve specific strain magnitudes within the channel. We defined the bending angle as being the angle from beneath the device to its outer edge with respect to the horizontal plane [Fig. 3(c), inset]. For 5% and 10% target strain, the model informed us to apply a bending angle of 9.8° and 19.2°, respectively [Fig. 3(c)]. Moreover, due to the linear relationship between strain and bending angle below 20°, we can apply controlled loading sequences of varying strains without varying the channel position. For example, we can alternate between 5% and 10% strain for each consecutive cycle or provide a 5% strain for 100 cycles before

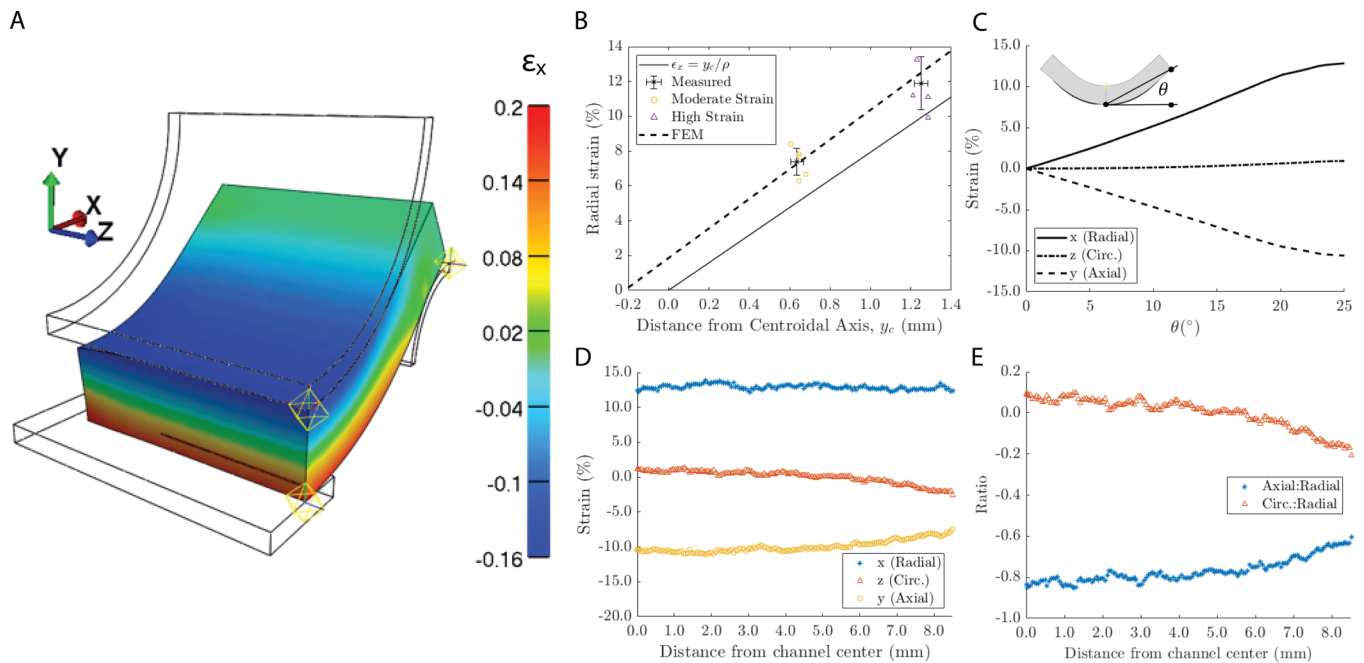


**FIG. 3.** (a) Quarter symmetrical color map of strain in the x-direction (radial strain) under maximum flexion. (b) Experimentally measured strains (open symbols) are plotted against the beam theory estimation (solid line) and the FE model (dashed line). Based on the model, the centroidal axis was offset from the neutral axis by 0.2 mm (difference in the intersection at the x axis). (c) Components of 3D strains, including radial, circumferential (circ.), and axial strains, are plotted for the element at the midpoint of the channel as the device is flexed from a flat starting position to a maximum angle based on the curvature of the barrel. Tensile and compressive strains were positive and negative, respectively. Radial, axial, and circ. strains correspond to x, y, and z strains. (d) Strains plotted along the channel demonstrated uniformity in the strain fields applied throughout the channel. Data are presented only for half of the channel due to symmetry. (e) Axial:radial and circumferential:radial strain ratios for the AoC were plotted along the length of the channel.

transitioning to applying a 10% strain for 100 cycles, and so on. The applied strain began to taper at 20°, which was due to the radius of curvature for the 3D printed barrel. For subsequent loading sequences, we utilized results from the model to modify the servo motor control sequence to ensure that the device applied 10% strain.

The model provided insights into strain uniformity along the channel length. We observed a change in strain and strain ratios toward the ends of the channel [Figs. 3(d) and 3(e)]. These changes are likely due to the tendency of the device to bend into a hyperbolic paraboloid shape, imposing a unique strain distribution that cannot be estimated with the pure beam bending assumption. The curvature becomes more pronounced toward edges of the device, resulting in strain deviations at  $\sim 2$  mm away from the center of the device. A more uniform strain distribution may be obtained by redesigning the device with a shorter channel to standardize applied strain along the full length of the channel. Alternatively, the device may be widened and the channel length maintained to create a uniform strain distribution while avoiding a reduction in cell population within the channel. Using the model, we can iterate on the AoC design and achieve target cell populations and applied strain distributions without the need for extensive lab time or fabrication.

### E. AF cell selection and culturing

Bovine AF cells were chosen for the AoC proof-of-concept testing due to accessibility and similarities with the human AF cells.<sup>15,48–52</sup> Static cell culture media was chosen instead of continuous flow to mimic AF tissue, which relies more on diffusion of nutrients than convection given its lack of vasculature.<sup>44</sup> To increase the reserve of nutrients without relying on convection, two pipet tips filled with 150  $\mu$ L of media were placed in each port hole and replaced every third day inside a cell culture hood like other microphysiological system designs.<sup>53</sup>

Prior to strain experiments, we confirmed using live/dead imaging that AF cells could sustain long-duration static culture [3-weeks; Fig. 4(a)] three times longer than required for a typical study. The highest resolution live/dead fluorescent image was captured only on the last day of culture to limit the stress on the cells while the sample was transferred to a microscope in a separate facility. Cells within the channel were found to be clustered near the ports, as expected, but also covered the remainder of the channel floor in a sparse monolayer. The number of living cells neared 2000 without any dead cells. However, it is possible that dead cells were washed from the channel when the live/dead solution was added. Only a few cells were positioned just above the sparse monolayer by adhering to corner surfaces between the channel floor and sidewalls. Seventy percent of manufactured devices were used in the study; the other 30% of manufactured devices were removed from testing primarily because of manufacturing defects, which included delamination of PDMS layers. Bubbles in the channel, a low cell population ( $\sim 300$  cells), and channel occlusion due to cell clumping were other, less frequent reasons to remove devices from testing. Future work will focus on reducing these losses.

The effects of a protein coating on cell adhesion in the channel were considered during chip development. In the channel, fibronectin coated PDMS at various concentrations (0, 0.03, 0.06, 0.125, 0.25, and 0.5 mg/ml) was compared to the plasma treated PDMS. Cell adhesion for each treatment was determined by observing the number of cells that adhered in the channel before spreading one hour, one day, three days, and seven days after. As far as cell adhesion and spreading, fibronectin performed similarly to plasma treated PDMS in the channel (Fig. S2B in the [supplementary material](#)). While fibronectin may play an important role in cell adhesion in the presence of excessive loading, it was eliminated from the protocol for simplicity at this stage.

We did not design the surface of the PDMS channel to include select areas for cell attachment; thus, cells were able to multiply during the culture period. The cell population was observed

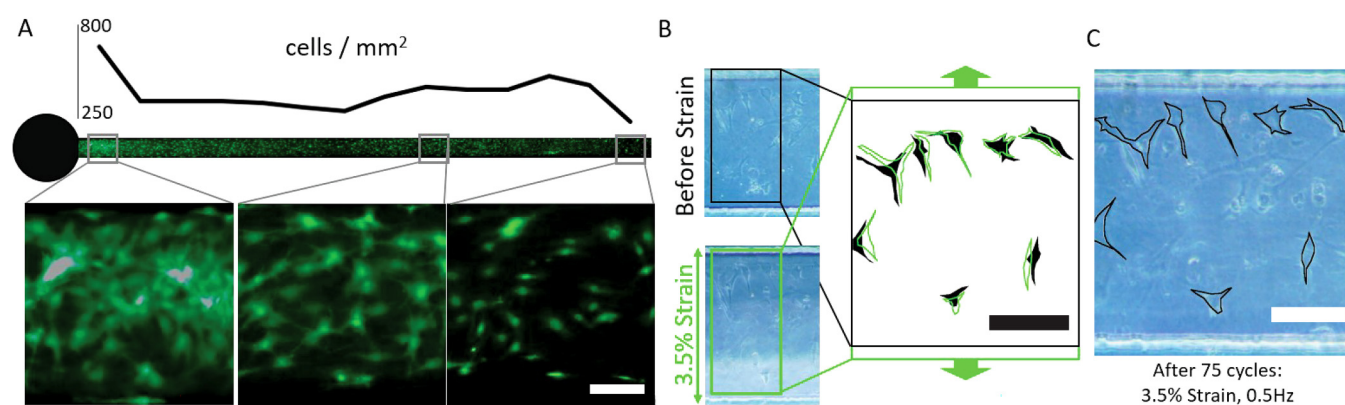


**FIG. 4.** (a) Live/dead staining of an AF cell population (nearly 2000 cells/channel) after three weeks of culture. Cell density varied throughout the channel with the greatest number near the media port (black circle). The other half of the channel had a similar distribution of cells so only one half of the channel was shown. Scale bar = 100  $\mu$ m. (b) Cells with sufficient contrast were segmented with polygon selections to compare before and during strain. Scale bar = 100  $\mu$ m. (c) A brightfield image was taken after strain was applied to confirm that cells remained attached to the channel for at least an hour after loading. Polygon selections are included to distinguish each cell. Scale bar = 100  $\mu$ m = 100  $\mu$ m.

multiplying over multiple days using brightfield images until a high confluency was reached and maintained (Fig. S2A in the [supplementary material](#)).

While the cell population of the current design is too low for sufficient RNA yield for gene expression analysis, the device dimensions can be scaled to increase cell population while maintaining similar strain profiles. The devices can also be pooled to accumulate the required number of cells for the analysis.

### F. Applying cyclic load to AF cells in the device

To establish the feasibility of the AoC as a platform for studying cell mechanobiology within load-bearing tissues, we seeded the device's microchannel with a sparse population of bovine AF cells (hundreds of cells) to limit any effects of population size on cellular strain. While a greater cell density could be used, such that more cell-cell interactions occur, a consistent cell density should be used between treatment groups. We allowed the cells to proliferate for 3 days before applying cyclic loading. A strain of 3.5% at 0.5 Hz for 75 cycles was chosen to represent low physiological loading.<sup>54</sup> We took brightfield images of the channel before loading, with applied strain, and after the cyclic loading. By processing the brightfield images with ImageJ, we observed cell deformity and strains in parallel (radial) and perpendicular (circumferential) directions relative to the channel. Despite the lower resolution ( $10\times$  objective lens), consistent differences can be seen in annotated brightfield images of the cells between the strained and unstrained channel [Fig. 4(b)]. However, with our initial study looking at cells during chip deformation, we did not observe significant cell migration and the image resolution was not sufficient to track cell deformations. However, we think that such a system can be used with better imaging facilities to study cell behaviors with loading. An additional brightfield image was taken after strain was applied to confirm that cells remained adhered to the channel for at least an hour after loading [Fig. 4(c)]. Meanwhile, static devices were used as controls to identify changes to cell viability, migration, and morphology due to the cell microenvironment within the chip. Cell migration was observed without mechanical loading (Fig. S3 in the [supplementary material](#)), which will need to be considered when measuring cell changes under mechanical load.

### G. Limitations

The AoC has been proven to be durable and effective at applying physiological strains within 0%–10%. However, *in situ* strains in the AF can be hyperphysiological (15%–20% and greater).<sup>26–28,32,46</sup> Strains in the 15%–20% range are achievable on the AoC by either decreasing the radius of curvature,  $\rho$  or the distance,  $y_c$  [Fig. 2(c)]. However, additional long-term cyclic testing is needed to evaluate device durability given these higher strains.

Furthermore, to measure strains more accurately than with brightfield images, a reference and a deformed image can be acquired using fluorescent protein tags or live cell dyes (e.g., live/dead or f-actin). Digital image correlation can then convert these images to strain maps. While we detected morphological differences in strained vs unstrained bovine AF cells, measuring these differences and converting them to strains maps using digital image correlation remains challenging due to low-contrast images. Ongoing work is focused on

establishing high-contrast images, which would enable digital image correlation as well as automatic, live-cell segmentation.

It should also be noted that cell access to nutrients depends on position along the length of the channel, which may play a role in viability as well as response to loads. For this reason, cell position will be taken into account as a possible variable in the future.

Additionally, the throughput in terms of cells and test replicates are limited. For a higher throughput of cells per device, all dimensions can be scaled to increase the volume and surface area of the channel while still creating a similar strain environment. For a higher throughput of tests, multiple devices with the existing dimensions could be placed in an array and actuated simultaneously.

Also, while culturing cells in the current design, pipet tips acting as media reservoirs are open to the air, which increases the possibility of contamination. To mitigate the risk of contamination, filtered or barrier pipet tips can be used instead of traditional pipet tips so as to close off the external environment while still allowing for any changes in pressure.

Lastly, while bovine AF cells were cultured in the AoC channel in a monolayer for proof of concept, 3D cultures and therefore 3D loading conditions have yet to be explored with bovine cells or human cells. Upcoming challenges include introducing and adhering cell-gel constructs within the channel to the PDMS surface, and visualizing 3D strains under microscopy. A gel adds complexity as it limits the diffusion of nutrients, waste, and gas; but this effect can be mitigated by perfusion channels. Tools and techniques exist for addressing each of these concerns as the AoC matures in complexity and capability. Functionalization of the PDMS surface<sup>55,56</sup> can facilitate the cell-substrate adhesion and ensure proper force transfer from the surface to the construct. Visualizing fluorescently tagged actin within the cells using confocal microscopy can allow for 3D strain measurements on the cells. Computational modeling can predict the effects of perfusion channel dimensions and spacing on diffusion and loading before upgrades are made to the existing proof of concept. This ongoing work is founded upon the present proof-of-concept study to validate the physiological relevance of the AoC.

### III. CONCLUSION

We designed, modeled, and fabricated a flexing organ-chip, referred to as the flexing annulus-on-a-chip, or AoC. Our chip was designed to replicate complex loading observed in the intervertebral disc to study AF mechanobiology. We also conducted preliminary cell-based experiments to show that a population of cells could be maintained within a confined PDMS channel with limited nutrient flow.

Biological treatments to delay or prevent early onset of degeneration have been limited.<sup>57,58</sup> A platform or microphysiological system, which can replicate conditions of early to moderate disc degeneration could enable rapid testing of cellular therapies, drugs, or biomaterial-based treatments. The AoC's design provides a mechanism to study cell responses to loading such as orientation, gene expression, and response to drugs added to the culture media. Furthermore, the AoC could be used to model most load bearing annular structures, such as cardiovascular vessels, lymphatic vessels, and the cervix. The device design and loading mechanism provides a platform for tailoring applied dynamic strains.



From the computational modeling perspective, we seek to quantify the strains at localized regions within the cell monolayer encased in the channel using image processing. This high-resolution strain data would enable us to correlate the strain distribution across the microchannel with cell behavior such re-orientation, spreading, proliferation, or apoptosis. Moreover, it would allow us to create descriptive computational models to investigate cell biomechanics, including the potential to estimate cell elasticity and identify loading modalities that lead to cell softening and stiffening.<sup>59</sup> Taken together, these experimental and computational approaches would inform our understanding of AF cell mechanobiology and potentially identify the initiation and development of disc degeneration. Future work will investigate the response of human AF cells within the device as well as 3D cell-laden constructs.

## IV. METHODS

### A. Device fabrication

Each AoC device consisted of a 17 mm-long, straight rectangular channel ( $300 \times 50 \mu\text{m}^2$ ) with circular ports on either end [0.5 mm diameter; Fig. 1(b)]. A mylar photomask printed at 10 K dpi was created after designing the channel in AutoCAD (AUTODESK, San Rafael; Fig. S4 in the [supplementary material](#)). Standard single-step photolithography was used to create the master mold with a channel comprised of SU-8 (3050) spin coated onto a 4-in. silicon wafer at a thickness of  $50 \mu\text{m}$  (first 500 rpm for 10 s with 300 rpm/s, then 3300 rpm for 30 s with 300 rpm/s, Kayaku Advanced Materials, Westborough, MA). The SU-8 was baked for 14 min at  $95^\circ\text{C}$  before being exposed to  $160 \text{ mJ}/\text{cm}^2$  of UV (Karl Suss MA6) and baking for 4.5 min at  $95^\circ\text{C}$ . A SU-8 developer was used for 5.5 min to develop the partially cured SU-8 on a lab shaker. The SU-8 was then hard baked at  $200^\circ\text{C}$  for 30 min. By replica molding polydimethylsiloxane (PDMS; Sylgard 184 kit, Dow Chemical, Midland, MI) at a 10:1 ratio of base-to-crosslinker, a slab of PDMS was created with a channel featured on one side.

To achieve a desired thickness, PDMS was poured by weight onto the silicon wafers surrounded by aluminum foil and placed atop a large, leveled hotplate. The thicknesses of both slabs were controlled ( $\pm 0.05 \text{ mm}$ ) to dictate the position of the channel. The PDMS layer thicknesses ranged from 0.5 to 3.5 mm with a constant stacked thickness of 4 mm depending on the desired strain magnitude. PDMS was cured at  $60^\circ\text{C}$  overnight on the hotplate before being removed with a razor blade and covered with plastic wrap until further processing. After punching 0.5 mm diameter ports at either end of the channel, the molded PDMS slab was bonded to a second flat PDMS slab using oxygen plasma. Within seconds of the oxygen plasma treatment (using 70 SCCM oxygen with 21 W at 0.6 Torr pressure for 30 s), the PDMS slabs were pressed lightly together by hand and kept at room temperature. Cells suspended in media, as described below, were added to the channel within 20 min of bonding.

### B. Loading mechanism and device actuation

Readily available components such as Power HD 3001HB servo motors, an Arduino UNO microcontroller, and an external

3 A, 5 V power supply were chosen for the loading mechanism. These components were secured with fasteners to a base cut from aluminum with a waterjet cutter.

The AoC device was designed to conform to a 3D printed barrel structure fastened to the base, which was anchored to the microscope table. Critical dimensions for the 3D printed barrel structure including its viewing port for microscopy can be found in Fig. S5 in the [supplementary material](#). A polypropylene “packing” tape (Fig. S6 in the [supplementary material](#)) cradles the device and connects it to servo motor horns with pin joints to flex the AoC against the barrel structure [Figs. 2(a) and 2(b)]. These pin joints can be made with simple bolts inside plastic cylinders. As the servo horns rotate upward, the tape forces the device to conform to the barrel structure with a radius of 10 mm (designed in SOLIDWORKS and printed with PolyLatic acid on a CreaLity Ender 3 Pro). When the servo horns rotate downward, the device relaxes into a flat configuration. Throughout actuation, the device is fixed between the 3D printed barrel and a standard 1 mm glass slide. Thus, the channel is kept at a constant focal length from the objective lens. Frequency can be controlled between 0.5 and 2 Hz.

A FlexiForce load sensor (Tekscan, Boston, MA) was placed between the glass slide and the device without blocking the viewing port to ensure that the applied pressure was consistent and repeatable during installation and operation. Additionally, reference marks on the 3D printed barrel structure were used to reliably align the device during installation within several microns of the channel center. All loading was applied at room temperature ( $22^\circ\text{C}$ ).

### C. Strain measurement of the device channel

Experimentally, radial strain was measured by imaging the channel before and after bending with a  $10\times$  objective lens on an Olympus CKX31 microscope. Images were acquired before and after applied strain and the channel width was measured in the reference and deformed image using an automated script (MATLAB, MathWorks Inc.). Based on beam bending theory, we fabricated five “moderate” and five “high” strain configurations to represent the physiological range of radial strains reported. Therefore, the moderate and high strain groups were set to 5% and 10%, respectively. We optically tracked the motion of the channel walls under brightfield microscopy and used image processing to measure the applied strain across the channel width (i.e., radial strains). Radial strains were calculated as engineering strain by dividing the change in channel width during loading by the initial channel width measured in the reference configuration. To assess experimental repeatability, 30 sequential measurements were acquired to assess changes in loading over an extended period of time. This loading sequence was considered to be a single set, which was repeated three times (total of 90 data points) per device to assess repeatability of measurements acquired after uninstalling and reinstalling the AoC.

To confirm that devices could physically withstand extended loading, an accelerated life test was conducted by cyclically loading devices ( $n = 3$ ) for 66 K cycles. The devices and the loading mechanism were visually inspected by eye before and after accelerated life testing for signs of wear or crack propagation.

#### D. Finite element modeling and simulation of devices

We used a neo-Hookean constitutive model to describe the PDMS device because of its non-linear hyperelastic stress-strain behavior. The strain-energy function was defined as

$$W = \frac{\mu}{2}(\mathbf{I}_1 - 3) - \mu \ln \mathbf{J} + \frac{\lambda}{2}(\ln \mathbf{J})^2,$$

where  $\mathbf{I}_1$  is the first invariant of the right Cauchy–Green deformation tensor,  $\mu$  is the bulk modulus for small deformations,  $\lambda$  is the shear modulus for small deformations, and  $\mathbf{J}$  is the determinant of the deformation gradient tensor.<sup>60</sup> Material property calibration was conducted in FEBio Studio 1.3<sup>61</sup> by modeling a specimen under tension using ASTM D412 standards and data in the literature.<sup>62</sup> The PDMS was calibrated to have an elastic modulus of 1.7 MPa and a Poisson's ratio of 0.49 (Fig. S7 in the [supplementary material](#)). The constitutive model deviated from the experimental results by 0.2% and 3.4% relative error at the target channel strains of 5% and 10%, respectively.

Models for the AoC were created in SOLIDWORKS (Dassault Systemes) with the channel positioned for three target strain configurations, including 0%, 5%, and 10% radial strain based on beam theory estimations. For these configurations, the channel was placed at 0.00, 0.63, and 1.26 mm below the neutral axis [assumed to be identical to the centroidal axis; Fig. 2(c)], respectively. Each of the three models were imported into FEBio Studio and meshed with 266 K first-order tetrahedral elements (Fig. S8 in the [supplementary material](#)).

For the boundary conditions, we enforced zero-displacement in the direction normal to each symmetry plane of the chip, fixed the rigid barrel and microscope slide in place (Fig. S9 in the [supplementary material](#)), and defined sliding contacts between the rigid surfaces and the chip. A  $y$ -displacement of 7 mm was applied to the end of the device using a rigid deflector, replicating the function of the tape in a computationally stable manner. This condition forced the device's curvature during the test cycle, starting from when the device begins to bend until it reaches its maximum curvature. Model-predicted device curvature was verified with the experimental setup by overlaying images of the device in the deformed condition with the model output (Fig. S10 in the [supplementary material](#)). Strains ( $\epsilon$ ) in the  $x$ -,  $y$ -, and  $z$ -directions corresponding to radial, axial, and circumferential strains, respectively, were evaluated along the length of the channel. Lab-based strain measurements were limited to a 1.5 mm distance from the channel center therefore model results were compared at the same location only. A mesh convergence analysis was then conducted for the 10% strain configuration to confirm stability of the model results within the 1.5 mm window (Fig. S11 in the [supplementary material](#)). The percent error between the model's prediction and empirical measurements was calculated. 3D strain levels were compared to native AF tissue strains to confirm physiological relevance.

#### E. AF cell sourcing

Primary bovine AF cells were obtained by harvesting four discs from a single fresh oxtail (18–24 months old) obtained from the local abattoir. The outer AF was separated from the inner AF

and removed from the disc with a scalpel.<sup>63</sup> Outer AF cells, which are made up of only a single cell type were isolated through an 11-h digestion with collagenase type IV (Worthington Biochem) in serum media supplemented with buffers to maintain pH. Isolated cells were expanded in T75 flasks with DMEM supplemented with 10% FBS and 1% penicillin/streptomycin (PS/AM; GIBCO, Texas). At 90% confluency, cells were passaged using 0.05% Trypsin (CORNING, New York). Cells were transferred to the AoC devices between passages 3 and 8.

#### F. AF cell culturing in the device channel

After bonding the PDMS slabs to create the enclosed channel, the channel was rinsed with 70% ethanol then flushed and kept filled with de-ionized water. Then, 2.5  $\mu$ l of the suspended cell solution was pipetted into the channel at an approximate concentration of either  $2 \times 10^6$  or  $10 \times 10^6$  cells/ml. DMEM media supplemented with 20% FBS were used for AoC cultures to enhance cell proliferation.<sup>64</sup> The higher concentration of cells was used to evaluate the highest cell population achievable, while the lower cell concentration ( $2 \times 10^6$  cells/ml) was used for cell segmentation with brightfield imaging. Being careful not to introduce air bubbles, a droplet of media was added on top of each port hole to limit evaporation in the channel. The device with cells was then incubated in static conditions until AF cells adhered and showed signs of spread morphology (75 min).

An additional 300  $\mu$ l of cell culture media was split between two pipet tips and inserted on either end of the channel to act as reservoirs (VWR 20uL LTS compatible 76323-944). Right before the pipet tips were inserted into the portholes, several microliters of media were pushed to the end of the tip to form a droplet that could form a fluidic connection with the channel without introducing bubbles. Given equal volumes of media in each reservoir, fluid in the channel remained static, which left only diffusion for nutrient and waste transport. All devices were housed in optically clear containers within the incubator, which was kept at 37 °C and 5% CO<sub>2</sub>. Fresh media was added every third day by replacing the pipet tips with new ones and refilling them with new media. Convection of cell media occurs if the device is tilted for an extended period of time due to a differential in media height between pipet tips. For this reason, the devices were held and stored flat.

Prior to applying cyclic loading, devices that presented the following were removed from the study: bubbles within the channel, channels with fewer than  $\sim 300$  cells, clumps of cell occluding the channel, delamination of PDMS layers, or contamination. Just prior to loading, the chip itself and loading device surfaces in contact with the chip were wiped with 70% ethanol.

#### G. AF cell cyclic loading

For initial testing with the AoC, mechanical loading was performed outside of an incubator at room temperature (22 °C). Devices were loaded for a total of 75 cycles with 3.5% engineering strain at 0.5 Hz as a physiologically relevant proof of concept. For initial studies, we chose a low level of physiological strain to ensure cell damage or detachment did not occur. We also chose a low cycle count to limit any adverse effects on cell health due to loading at room temperature (loading time < 5 min, based on the

average time for changing media). Further tests are needed to better understand the impact of longer duration testing at room temperature (i.e., > 5 min). However, the loading platform is small ( $15 \times 15 \times 4.4 \text{ cm}^3$ ) enough that the entire device could be placed in the incubator for longer duration testing. Alternatively, the loading platform could be redesigned to work with a hot plate. Pipet tips with reservoirs of media were left plugged in during loading. Brightfield images of the cells in the channel were acquired before, during, and immediately following loading. These images were then processed using ImageJ.

#### H. Image processing and preliminary analysis

Using the lower concentration of  $2 \times 10^6$  cells/ml, cells were cultured within the channel for cell segmentation. Brightfield images of nine cells before strain and after strain within the channel were imported into ImageJ. Using custom polygons, we traced cells in images acquired before, after, and during stretching to demonstrate our ability to segment cells without fluorescent markers.

#### I. Long-term *in vitro* cell viability

Cell viability was evaluated at three weeks for the long-term cell culture study using the Live/Dead Viability/Cytotoxicity kit for mammalian cells using the manufacturer's instructions (Live/Dead Life Technologies Corporation, Eugene, OR). Rather than flush the channel, the live/dead solution was fed into the channel with gravity to minimize shear forces using a  $10 \mu\text{l}$  pipet tip with  $5 \mu\text{l}$  of live/dead solution. After a 30-min incubation, the first pipet tip was removed and a second larger ( $20 \mu\text{l}$ ) pipet tip filled with phosphate buffered saline (PBS) was inserted. PBS remained in the channel throughout imaging.

#### SUPPLEMENTARY MATERIAL

See the [supplementary material](#) for the results from computer models, images of cells at various time points within the device, computer aided design (CAD) images with dimensions for critical parts of the annulus-on-a-chip, the mask design used for photolithography, PDMS material properties, and convergence data for the computer models.

#### ACKNOWLEDGMENTS

Special thanks to Jessica Herrera for wet lab technical support, Minhao Zhou for guidance on modeling with FEBio Studio, and Rahul Malayappan for creating and rendering [Fig. 1\(d\)](#).

#### AUTHOR DECLARATIONS

##### Conflict of interest

The authors have no conflicts to disclose.

##### Author Contributions

**Jonathan P. McKinley:** Conceptualization (equal); Data curation (equal); Formal analysis (equal); Investigation (equal); Methodology (equal); Project administration (equal); Resources (equal); Software (equal); Supervision (equal); Validation (equal); Visualization

(equal); Writing – original draft (equal); Writing – review & editing (equal). **Andre R. Montes:** Data curation (equal); Formal analysis (equal); Investigation (equal); Methodology (equal); Resources (equal); Software (equal); Supervision (equal); Validation (equal); Visualization (equal); Writing – original draft (equal); Writing – review & editing (equal). **Maple N. Wang:** Data curation (supporting); Formal analysis (supporting); Software (supporting). **Anuya R. Kamath:** Data curation (supporting); Investigation (supporting); Resources (supporting). **Gissell Jimenez:** Resources (supporting); Software (supporting). **Jianhua Lim:** Data curation (equal); Software (equal). **Siddharth A. Marathe:** Data curation (supporting); Software (supporting). **Mohammad R. K. Mofrad:** Supervision (equal); Writing – review & editing (equal); **Grace D. O'Connell:** Conceptualization (equal); Formal analysis (equal); Project administration (equal); Resources (equal); Supervision (equal); Writing – original draft (equal); Writing – review & editing (equal).

#### DATA AVAILABILITY

The data that support the findings of this study are available from the corresponding author upon reasonable request.

#### REFERENCES

- 1K. Luoma, H. Riihimäki, R. Luukkonen, R. Raininko, E. Viikari-Juntura, and A. Lamminen, "Low back pain in relation to lumbar disc degeneration," *Spine* **25**, 487–492 (2000).
- 2T. Vos, A. D. Flaxman, M. Naghavi, R. Lozano, C. Michaud, M. Ezzati, K. Shibuya, J. A. Salomon, S. Abdalla, V. Aboyans *et al.* "Years lived with disability (ylds) for 1160 sequelae of 289 diseases and injuries 1990–2010: A systematic analysis for the global burden of disease study 2010," *Lancet* **380**, 2163–2196 (2012).
- 3D. I. Rubin, "Epidemiology and risk factors for spine pain," *Neurol. Clin.* **25**, 353–371 (2007).
- 4J. N. Katz, "Lumbar disc disorders and low-back pain: Socioeconomic factors and consequences," *JBJS* **88**, 21–24 (2006).
- 5M. Von Korff, R. A. Deyo, D. Cherkin, and W. Barlow, "Back pain in primary care. Outcomes at 1 year," *Spine* **18**, 855–862 (1993).
- 6A. C. Schwarzer, C. N. Aprill, R. Derby, J. Fortin, G. Kine, and N. Bogduk, "The prevalence and clinical features of internal disc disruption in patients with chronic low back pain," *Spine* **20**, 1878–1883 (1995).
- 7A. White and M. Panjabi, *Clinical Biomechanics of the Spine* (Lippincott, 1978).
- 8M. Rudert and B. Tillmann, "Lymph and blood supply of the human intervertebral disc: Cadaver study of correlations to discitis," *Acta Orthop.* **64**, 37–40 (1993).
- 9J. Urban, S. Roberts, and J. Ralphs, "The nucleus of the intervertebral disc from development to degeneration," *Am. Zool.* **40**, 53–61 (2000).
- 10M. Benoit, "Natural history of the aging spine," *Aging Spine* **12**, 4–7 (2005).
- 11M. Molinos, C. R. Almeida, J. Caldeira, C. Cunha, R. M. Gonçalves, and M. A. Barbosa, "Inflammation in intervertebral disc degeneration and regeneration," *J. R. Soc. Inter.* **12**, 20141191 (2015).
- 12N. M. Shahraki, A. Fatemi, A. Agarwal, and V. K. Goel, "Prediction of clinically relevant initiation and progression of tears within annulus fibrosus," *J. Orthop. Res.* **35**, 113–122 (2017).
- 13S. E. Bezci, B. Werbner, M. Zhou, K. G. Malollari, G. Dorhaci, C. Carraro, A. Streets, and G. D. O'Connell, "Radial variation in biochemical composition of the bovine caudal intervertebral disc," *JOR Spine* **2**, e1065 (2019).
- 14B. Yang and G. D. O'Connell, "Intervertebral disc swelling maintains strain homeostasis throughout the annulus fibrosus: A finite element analysis of healthy and degenerated discs," *Acta. Biomater.* **100**, 61–74 (2019).

- <sup>15</sup>G. D. O'Connell, W. Johannessen, E. J. Vresilovic, and D. M. Elliott, "Human internal disc strains in axial compression measured noninvasively using magnetic resonance imaging," *Spine* **32**, 2860–2868 (2007).
- <sup>16</sup>A. J. Rahyussalim, M. L. L. Zufar, and T. Kurniawati, "Significance of the association between disc degeneration changes on imaging and low back pain: A review article," *Asian Spine J.* **14**, 245 (2020).
- <sup>17</sup>B. Vernon-Roberts, N. L. Fazzalari, and B. A. Manthey, "Pathogenesis of tears of the annulus investigated by multiple-level transaxial analysis of the t12-l1 disc," *Spine* **22**, 2641–2646 (1997).
- <sup>18</sup>D. A. Reid and P. J. McNair, "Factors contributing to low back pain in rowers," *Br. J. Sports. Med.* **34**, 321–322 (2000).
- <sup>19</sup>B. Vernon-Roberts, R. J. Moore, and R. D. Fraser, "The natural history of age-related disc degeneration: The pathology and sequelae of tears," *Spine* **32**, 2797–2804 (2007).
- <sup>20</sup>T. M. Hosea and J. A. Hannafin, "Rowing injuries," *Sports Health* **4**, 236–245 (2012).
- <sup>21</sup>R. D. Abbott, A. K. Howe, H. M. Langevin, and J. C. Iatridis, "Live free or die: Stretch-induced apoptosis occurs when adaptive reorientation of annulus fibrosus cells is restricted," *Biochem. Biophys. Res. Commun.* **421**, 361–366 (2012).
- <sup>22</sup>W. M. Han, S. J. Heo, T. P. Driscoll, L. J. Smith, R. L. Mauck, and D. M. Elliott, "Macro- to microscale strain transfer in fibrous tissues is heterogeneous and tissue-specific," *Biophys. J.* **105**, 807–817 (2013).
- <sup>23</sup>H. Yang, S. Haldeman, M. L. Lu, and D. Baker, "Low back pain prevalence and related workplace psychosocial risk factors: A study using data from the 2010 national health interview survey," *J. Manipulative Physiol. Ther.* **39**, 459–472 (2016).
- <sup>24</sup>C. Neidlinger-Wilke, F. Galbusera, H. Pratsinis, E. Mavrogonatou, A. Mietsch, D. Kletsas, and H.-J. Wilke, "Mechanical loading of the intervertebral disc: From the macroscopic to the cellular level," *Eur. Spine J.* **23**, 333–343 (2014).
- <sup>25</sup>B. V. Fearing, P. A. Hernandez, L. A. Setton, and N. O. Chahine, "Mechanotransduction and cell biomechanics of the intervertebral disc," *JOR Spine* **1**, e1026 (2018).
- <sup>26</sup>S. Molladavoodi, J. McMorran, and D. Gregory, "Mechanobiology of annulus fibrosus and nucleus pulposus cells in intervertebral discs," *Cell Tissue Res.* **379**, 429–444 (2020).
- <sup>27</sup>L. Ning, L. Gao, F. Zhang, X. Li, and T. Wang, "Mechanical stretch induces annulus fibrosus cell senescence through activation of the rhoa/rock pathway," *BioMed. Res. Int.* **2021**, 2021 (2021).
- <sup>28</sup>E. Cambria, M. J. Arlt, S. Wandel, O. Krupkova, W. Hitzl, F. S. Passini, O. N. Hausmann, J. G. Snedeker, S. J. Ferguson, and K. Wuertz-Kozak, "Trpv4 inhibition and crispr-cas9 knockout reduce inflammation induced by hyperphysiological stretching in human annulus fibrosus cells," *Cells* **9**, 1736 (2020).
- <sup>29</sup>H. Pratsinis, A. Papadopoulou, C. Neidlinger-Wilke, M. Brayda-Bruno, H.-J. Wilke, and D. Kletsas, "Cyclic tensile stress of human annulus fibrosus cells induces mapk activation: Involvement in proinflammatory gene expression," *Osteoarthritis Cartilage* **24**, 679–687 (2016).
- <sup>30</sup>H.-Y. Hsieh, G. Camci-Unal, T.-W. Huang, R. Liao, T.-J. Chen, A. Paul, F.-G. Tseng, and A. Khademhosseini, "Gradient static-strain stimulation in a microfluidic chip for 3d cellular alignment," *Lab. Chip.* **14**, 482–493 (2014).
- <sup>31</sup>B. L. Showalter, J. F. DeLucca, J. M. Peloquin, D. H. Cortes, J. H. Yoder, N. T. Jacobs, A. C. Wright, J. C. Gee, E. J. Vresilovic, and D. M. Elliott, "Novel human intervertebral disc strain template to quantify regional three-dimensional strains in a population and compare to internal strains predicted by a finite element model," *J. Orthop. Res.* **34**, 1264–1273 (2016).
- <sup>32</sup>D. Amin, C. Moawad, and J. Costi, "New findings confirm regional internal disc strain changes during simulation of repetitive lifting motions," *Ann. Biomed. Eng.* **47**, 1378–1390 (2019).
- <sup>33</sup>C. L. Thompson, S. Fu, H. K. Heywood, M. M. Knight, and S. D. Thorpe, "Mechanical stimulation: A crucial element of organ-on-chip models," *Front. Bioeng. Biotechnol.* **8**, 1426 (2020).
- <sup>34</sup>A. Mainardi, E. Cambria, P. Occhetta, I. Martin, A. Barbero, S. Schären, A. Mehrkens, and O. Krupkova, "Intervertebral disc-on-a-chip as advanced *in vitro* model for mechanobiology research and drug testing: A review and perspective," *Front. Bioeng. Biotechnol.* **9**, 1–18 (2021).
- <sup>35</sup>H. A. L. Guerin and D. M. Elliott, "Degeneration affects the fiber reorientation of human annulus fibrosus under tensile load," *J. Biomech.* **39**, 1410–1418 (2006).
- <sup>36</sup>G. D. O'Connell, E. J. Vresilovic, and D. M. Elliott, "Human intervertebral disc internal strain in compression: The effect of disc region, loading position, and degeneration," *J. Orthop. Res.* **29**, 547–555 (2011).
- <sup>37</sup>G. D. O'Connell, H. L. Guerin, and D. M. Elliott, "Theoretical and uniaxial experimental evaluation of human annulus fibrosus degeneration," *J. Biomech. Eng.* **131**, 111007 (2009).
- <sup>38</sup>N. Berger-Roscher, G. Casaroli, V. Rasche, T. Villa, F. Galbusera, and H.-J. Wilke, "Influence of complex loading conditions on intervertebral disc failure," *Spine* **42**, E78–E85 (2017).
- <sup>39</sup>M. Zhou, R. D. Huff, Y. Abubakar, and G. D. O'Connell, "Torque- and muscle-driven flexion induce disparate risks of *in vitro* herniation: A multiscale and multi-phasic structure-based finite element study," *J. Biomech. Eng.* **144**, 061005 (2022).
- <sup>40</sup>K. Kaarj and J. Y. Yoon, "Methods of delivering mechanical stimuli to organ-on-a-chip," *Micromachines* **10**, 700 (2019).
- <sup>41</sup>D. Lee, A. Erickson, T. You, A. T. Dudley, and S. Ryu, "Pneumatic microfluidic cell compression device for high-throughput study of chondrocyte mechanobiology," *Lab. Chip.* **18**, 2077–2086 (2018).
- <sup>42</sup>P. Occhetta, A. Mainardi, E. Votta, Q. Vallmajo-Martin, M. Ehrbar, I. Martin, A. Barbero, and M. Rasponi, "Hyperphysiological compression of articular cartilage induces an osteoarthritic phenotype in a cartilage-on-a-chip model," *Nat. Biomed. Eng.* **3**, 545–557 (2019).
- <sup>43</sup>F. Marchand and A. M. Ahmed, "Investigation of the laminate structure of lumbar disc annulus fibrosus," *Spine* **15**, 402–410 (1990).
- <sup>44</sup>C. M. De Geer, "Intervertebral disk nutrients and transport mechanisms in relation to disk degeneration: A narrative literature review," *J. Chiropr. Med.* **17**, 97–105 (2018).
- <sup>45</sup>A. Rohlmann, T. Consmüller, M. Dreischarf, M. Bashkuev, A. Disch, E. Pries, G. N. Duda, and H. Schmidt, "Measurement of the number of lumbar spinal movements in the sagittal plane in a 24-hour period," *Eur. Spine J.* **23**, 2375–2384 (2014).
- <sup>46</sup>M. Likhitanichkul, O. M. Torre, J. Gruen, B. A. Walter, A. C. Hecht, and J. C. Iatridis, "Do mechanical strain and TNF- $\alpha$  interact to amplify pro-inflammatory cytokine production in human annulus fibrosus cells?," *J. Biomech.* **49**, 1214–1220 (2016).
- <sup>47</sup>S. Dogru, B. Aksoy, H. Bayraktar, and B. E. Alaca, "Poisson's ratio of pdms thin films," *Polym. Test.* **69**, 375–384 (2018).
- <sup>48</sup>Z. Li, Y. Gehlen, F. Heizmann, S. Grad, M. Alini, R. G. Richards, D. Kubosch, N. Südkamp, K. Izadpanah, E. J. Kubosch *et al.*, "Preclinical ex-vivo testing of anti-inflammatory drugs in a bovine intervertebral degenerative disc model," *Front. Bioeng. Biotechnol.* **8**, 583 (2020).
- <sup>49</sup>M. Calió, B. Gantenbein, M. Egli, L. Poveda, and F. Ille, "The cellular composition of bovine coccygeal intervertebral discs: A comprehensive single-cell rna-seq analysis," *Int. J. Mol. Sci.* **22**, 4917 (2021).
- <sup>50</sup>J. Desrochers and N. A. Duncan, "Strain transfer in the annulus fibrosus under applied flexion," *J. Biomech.* **43**, 2141–2148 (2010).
- <sup>51</sup>G. D. O'Connell, E. J. Vresilovic, and D. M. Elliott, "Comparison of animals used in disc research to human lumbar disc geometry," *Spine* **32**, 328–333 (2007).
- <sup>52</sup>C. Daly, P. Ghosh, G. Jenkin, D. Oehme, and T. Goldschlager, "A review of animal models of intervertebral disc degeneration: Pathophysiology, regeneration, and translation to the clinic," *BioMed. Res. Int.* **2016**, 5952165 (2016).
- <sup>53</sup>B. Charrez, V. Charwat, B. A. Siemons, I. Goswami, C. Sakolish, Y.-S. Luo, H. Finsberg, A. G. Edwards, E. W. Miller, I. Rusyn *et al.*, "Heart muscle micro-physiological system for cardiac liability prediction of repurposed covid-19 therapeutics," *Front. Pharmacol.* **12**, 4 (2021).
- <sup>54</sup>G. Sowa, P. Coelho, N. Vo, R. Bedison, A. Chiao, C. Davies, R. Studer, and J. Kang, "Determination of annulus fibrosus cell response to tensile strain as a function of duration, magnitude, and frequency," *J. Orthop. Res.* **29**, 1275–1283 (2011).

- <sup>55</sup>Y. J. Chuah, Y. T. Koh, K. Lim, N. V. Menon, Y. Wu, and Y. Kang, "Simple surface engineering of polydimethylsiloxane with polydopamine for stabilized mesenchymal stem cell adhesion and multipotency," *Sci. Rep.* **5**, 1–12 (2015).
- <sup>56</sup>Y. J. Chuah, S. Kuddannaya, M. H. A. Lee, Y. Zhang, and Y. Kang, "The effects of poly (dimethylsiloxane) surface silanization on the mesenchymal stem cell fate," *Biomater. Sci.* **3**, 383–390 (2015).
- <sup>57</sup>J. Stergar, L. Gradisnik, T. Velnar, and U. Maver, "Intervertebral disc tissue engineering: A brief review," *Bosnian. J. Basic. Med. Sci.* **19**, 130–137 (2019).
- <sup>58</sup>G. Chu, C. Shi, H. Wang, W. Zhang, H. Yang, and B. Li, "Strategies for annulus fibrosus regeneration: From biological therapies to tissue engineering," *Front. Bioeng. Biotechnol.* **6**, 90 (2018).
- <sup>59</sup>C.-T. Chen and G. X. Gu, "Learning hidden elasticity with deep neural networks," *Proc. Natl. Acad. Sci.* **118**, 1–8 (2021).
- <sup>60</sup>L. Treloar, "The elasticity and related properties of rubbers," *Rep. Prog. Phys.* **36**, 755 (1973).
- <sup>61</sup>S. A. Maas, B. J. Ellis, G. A. Ateshian, and J. A. Weiss, "Febio: Finite elements for biomechanics," *J. Biomech. Eng.* **134**, 011005 (2012).
- <sup>62</sup>I. Johnston, D. McCluskey, C. Tan, and M. Tracey, "Mechanical characterization of bulk sylgard 184 for microfluidics and microengineering," *J. Micromech. Microeng.* **24**, 035017 (2014).
- <sup>63</sup>G. G. van den Akker, M. I. Koenders, F. A. van de Loo, P. L. van Lent, E. B. Davidson, and P. M. van der Kraan, "Transcriptional profiling distinguishes inner and outer annulus fibrosus from nucleus pulposus in the bovine intervertebral disc," *Eur. Spine J.* **26**, 2053–2062 (2017).
- <sup>64</sup>R. R. Khasawneh, A. H. A. Sharie, E. A.-E. Rub, A. O. Serhan, and H. N. Obeidat, "Addressing the impact of different fetal bovine serum percentages on mesenchymal stem cells biological performance," *Mol. Biology Rep.* **46**, 4437–4441 (2019).